

Exploration of magnetoelastic deformations in spin-chain compound CuBr_2

Biaoyan Hu,^{1,2,*} Yingying Peng,¹ Xiaoqiang Liu,¹ Qizhi Li,¹ Qiangqiang Gu,¹
Matthew J. Krogstad,³ Raymond Osborn,³ Takashi Honda,⁴ Ji Feng,¹ and Yuan Li¹

¹*International Center for Quantum Materials, Peking University, Beijing, China*

²*Quantum Science Center of Guangdong-Hong Kong-Macao Greater Bay Area, Shenzhen, China*

³*Materials Science Division, Argonne National Laboratory, Lemont, IL, USA*

⁴*Institute of Materials Structure Science, High Energy Accelerator Research Organization (KEK), Tokai, Ibaraki, Japan*

We investigate a spin- $\frac{1}{2}$ antiferromagnet, CuBr_2 , which has quasi-one-dimensional structural motifs. The system has previously been observed to exhibit unusual Raman modes possibly due to a locally deformed crystal structure driven by the low-dimensional magnetism. Using hard X-ray scattering and neutron total scattering, here we aim to verify a specific form of tetramerized lattice deformation proposed in the previous study. Apart from diffuse scattering signals which we can reproduce by performing a thorough modeling of the lattice's thermal vibrations, we do not observe evidence for a tetramerized lattice structure within our detection sensitivity. As a result, it is more likely that the unusual Raman modes in CuBr_2 arise from classical magnon-phonon hybridization, rather than from quantum spin-singlet-driven lattice deformation.

I. INTRODUCTION

Low-dimensional magnets command attention in scientific studies [1–5]. In these systems, long-range magnetic order weakens, giving rise to localized spin entanglement, including spin singlets, especially in spin- $\frac{1}{2}$ chain systems [6–9]. Introducing frustration transforms the antiferromagnetic chain, resulting in spiral spin order and the formation of intriguing spin singlets [10–12], which interact with the Néel state, as supported by theoretical studies and experimental evidence [13, 14].

The study of spin singlets is important, as they play a key role in forming the resonating valence bond (RVB) state, which is among the prominent explanations of high-temperature superconductivity [15–17]. Looking into spin singlets may help us better understand correlated electronic materials and quantum magnetism. Spin singlets have been identified in various low-dimensional magnets [18–21]. Recent Raman studies on a low-dimensional magnet CuBr_2 have also suggested potential signs of spin singlets [22]. This study aims to verify the spin singlets in CuBr_2 .

CuBr_2 is a quasi-one-dimensional spin- $\frac{1}{2}$ frustrated antiferromagnet. It crystallizes in the monoclinic space group $C2/m$ with lattice constants of $a \approx 7.2 \text{ \AA}$, $b \approx 3.5 \text{ \AA}$, $c \approx 7.0 \text{ \AA}$ and $\beta \approx 119.6^\circ$. CuBr_2 exhibits a Néel temperature (T_N) of 73.5 K [22–25]. Below T_N , CuBr_2 adopts a Néel state characterized by a spiral magnetic order, with a propagating wave vector of $\mathbf{q}_s = (1, 0.235, 0.5)$ in reciprocal lattice units (r.l.u.) [22, 26, 27]. The spin rotation between adjacent Cu ions along chains is approximately 85° due to the competition between the nearest-neighbor (J_1) and the next-nearest-neighbor (J_2) interaction [22, 26].

The Raman scattering spectrum of CuBr_2 revealed signals intriguing non-monotonic variations with temperature at specific energies, exhibiting a pronounced maximum near the Néel temperature T_N [22]. No-

tably, these unusual modes did not align with the phonon energies at Γ points, but coincided instead with the phonon energy at $\mathbf{Q} \approx 0.25 \mathbf{b}^*$ [22]. In an attempt to elucidate this phenomenon, two compelling explanations were proposed, one of which focusing on the hypothetical singlets. Given that antiferromagnetic J_2 is the dominant spin interaction among the three primary interactions (J_1 , J_2 , and J_3) [26], it has been proposed in the previous study that spin singlets might emerge within the next-nearest neighboring Cu pairs along chains [22], as represented in Fig. 1 (b). Consequently, spin interactions might revise on the lattice, leading to the tetramerized lattice deformation, which provided an explanation for the observed magnetoelastic coupling effect in the Raman experiments [22].

To experimentally verify the existence of tetramers in CuBr_2 , scattering experiments are undertaken. These experiments involve an analysis of both the momentum distribution of the intensity and the pair distribution function (PDF). By analyzing momentum distribution intensity and studying the PDF, we aim to provide evidence and insights into the potential tetramerized deformation in CuBr_2 . These experiments would enhance our grasp of quantum magnetism.

We conduct a detailed hard X-ray scattering experiment on a pristine CuBr_2 single crystal to investigate the atomic displacements potentially induced by tetramers. Leveraging the force constants obtained from density functional theory (DFT), we calculate the thermal diffuse scattering (TDS). The TDS intensity is calculated and show agreement with the experimental data, offering no indication of the presence of tetramers.

In order to explore the possibility of highly randomized tetramers, we perform an extensive analysis of the PDFs derived from neutron total scattering measurements on CuBr_2 powder. However, despite a thorough examination, we do not detect any distinc-

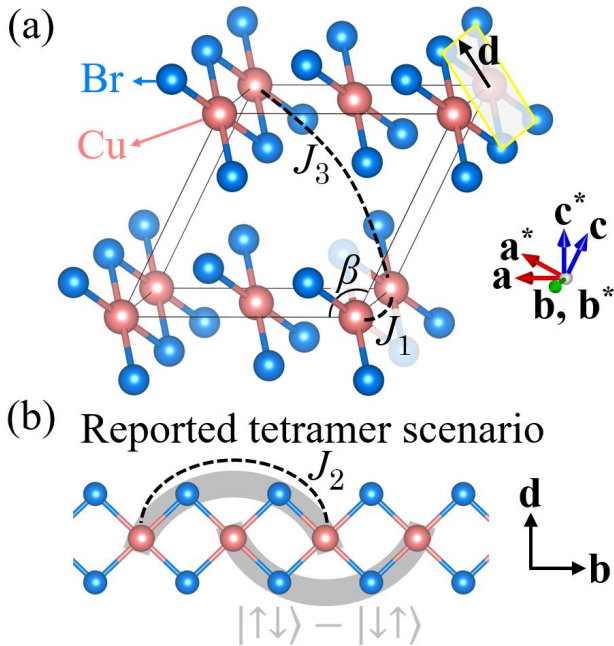


FIG. 1. (a) Crystal structure of CuBr_2 . Here vector \mathbf{d} is defined as shown, which is approximately parallel to $(\mathbf{a}+\mathbf{c})$. (b) The diagram of the reported tetramer scenario in the previous study [22]. The grey curve connected two Cu atoms is a spin singlet. In this scenario, two singlets may form a tetramer.

tive variations in the nearest Cu-Cu pairs, thus reinforcing the conclusion that tetramers are not present in our study.

These findings imply a higher likelihood that the unusual Raman modes observed in CuBr_2 result from classical magnon-phonon hybridization, rather than being driven by quantum spin-singlet-induced lattice deformation.

II. METHODS

A. Sample preparation

The growth of the CuBr_2 single crystal involve a controlled process of slow evaporation. Initially, a saturated solution of CuBr_2 is prepared and placed in a dry and stable environment at room temperature. With great care, the solution is allowed to gradually evaporate until it reaches complete dryness, resulting in the formation of high-quality sub-centimeter single crystals. Throughout this process, it is essential to strictly avoid any form of heating, as it could lead to the undesirable production of CuBr and compromise the purity of the sample.

In order to ensure the utmost accuracy of the PDF data, a procedure is employed to obtain high-quality CuBr_2 powder. The saturated CuBr_2 solution is subjected to a freeze-drying technique, which effec-

tively precipitate the CuBr_2 compound in a crisp and sponge-like form. By gently crushing the sponge-like CuBr_2 , powder is obtained with exceptional purity, well-defined crystallinity, and a satisfactory random orientation. These attributes are essential for the intended analysis and characterization of the material.

B. Hard X-ray scattering

A hard X-ray scattering experiment is conducted on a CuBr_2 single crystal to unravel the fine atomic structure. X-rays are chosen as the primary investigative tool due to their precision in targeting and analyzing non-magnetic signals.

In the hypothesis of minor lattice deformations, their influence on small momenta becomes negligible as long as these deformations are much smaller than the wavelength scale. Hard X-rays are essential for detecting subtle deformations and exploring large momentum transfers in this experiment, helping understand intricate structural changes in the crystal lattice.

The experimental setup, illustrated in Fig. 2, involves the penetration of 87-keV hard X-rays through the sample and subsequently scattered onto a rectangular detector screen. The detector array captures a specific section of the Ewald sphere corresponding to the sample's orientation. By rotating the sample, the Ewald sphere sweeps through the reciprocal space, generating a three-dimensional volume data set. Notably, the rotation axis is perpendicular to the initial X-ray direction.

To adequately cover the regions surrounding the \mathbf{b}^* axis in the reciprocal space, a deliberate slight angle is introduced between the crystal's \mathbf{b} axis and the rotation axis. The data collection process involves performing measurements at 31 different temperatures, spanning from 30 to 300 K. At each temperature, the sample holder is rotated by 0.1° increments, completing a full 360° rotation.

Considering the hypothetical scenario depicted in Fig. 1(b), the scattering intensity may exhibit superstructural signals which might manifest as a series of walls in the reciprocal space. For $\mathbf{Q} = h\mathbf{a}^* + k\mathbf{b}^* + l\mathbf{c}^*$, the potential superstructural signals might appear at $k = \mathcal{N}/4, \mathcal{N} \in \mathbb{Z}$. To identify the potential superstructural signals, it becomes necessary to calculate the TDS.

C. Calculation of thermal diffuse scattering

TDS is the coherent component of diffuse scattering, serving as a key element within it. TDS originates from the vibrations of atoms [28–30] and can

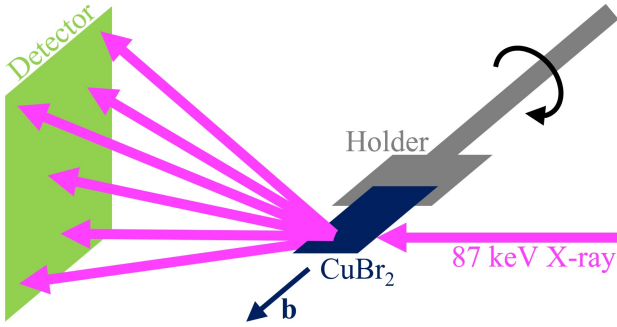


FIG. 2. Diagram of the hard X-ray scattering experiment. X-rays are transmitted through the CuBr_2 single crystal and scattered onto the detector screen. The sample holder rotates 360° around \mathbf{b} with the step of 0.1° .

be expanded as [28, 31]:

$$S_{\text{TDS}} = \sum_{p=1}^{\infty} S_p = \sum_{p=1}^n S_p + R_n, \quad (1)$$

in which S_p represents the p th-order TDS [28], corresponding to the scattering that involve the creation or annihilation of p phonons [31]. The remainder term R_n is defined as $R_n \equiv \sum_{p=n+1}^{\infty} S_p$, encompassing the contributions from higher-order terms beyond n .

To estimate the remainder term, we propose a model that incorporates random repositioning of each atom. This model provides a framework to calculate the remainder term R_n , which can be expressed as:

$$R_n \approx \frac{1}{\nu} \sum_{d=1}^{\nu} f_d^2 \left(1 - e^{-2W_d} \sum_{p=0}^n \frac{(2W_d)^p}{p!} \right). \quad (2)$$

Here, d represents the serial number of the atom within a primitive cell, while ν denotes the total number of atoms in a primitive cell, which is 3 for CuBr_2 . W_d represents the Debye-Waller factor. f_d corresponds to the atomic form factor, which employed in this work are sourced from the ionic data provided by Brown *et al.* [32].

To determine the accurate values of S_p and W_d , we utilize the force constant matrices obtained from DFT using Vienna *ab initio* simulation package (VASP) and Phonopy. To overcome the calculational challenge posed by infinite terms, the simplification of the remainder term R_n is essential for practical calculations.

D. Neutron total scattering

A neutron total scattering experiment is conducted at NOVA, J-PARC using 0.6 cm^3 of prepared CuBr_2 powder. The objective is to investigate changes in interatomic distances within the nucleus by analyzing the sample at different temperatures. Data within

the range of $1 \sim 34 \text{ \AA}^{-1}$ is selected and subjected to transformation for subsequent analysis.

The PDF $g(r)$ is calculated using the following equation [33, 34]:

$$g(r) = 1 + \frac{1}{2\pi^2 r \rho} \int_0^\infty \left(\frac{d\sigma/d\Omega}{N\langle b \rangle^2} - \frac{\langle b^2 \rangle}{\langle b \rangle^2} \right) \sin(Qr) Q dQ, \quad (3)$$

in which ρ represents the atomic number density, which is $0.039/\text{\AA}^3$ for CuBr_2 . $d\sigma/d\Omega$ corresponds to the differential scattering cross section, N denotes the number of atoms, b stands for the coherent scattering length, and $\langle \dots \rangle$ here indicates the average of all atoms. $g(r)$ provides the distribution of distances between pairs of atoms in the sample.

III. RESULTS

A. Hard X-ray scattering

In this study, we analyze the intensity of hard X-ray scattering on CuBr_2 by combining measurements with calculations. We aim to examine the impact of atomic displacements on the scattering behavior.

As previously mentioned, tetramerized deformation may result in additional scattering signals occurring at $k = N/4$. In Fig. 3(a)-(f), we illustrate three possible types of atomic displacements and the possible superstructural signals of each type. If atoms displace along \mathbf{b} , superstructural signals might be present with large k . Similarly, if atoms displace along \mathbf{d} , superstructural signals might be present with large \mathbf{Q}_d . Additionally, for displacements along both \mathbf{b} and \mathbf{d} , superstructural signals might be present with large momentum, either in terms of k or \mathbf{Q}_d .

We check the scattering intensity observed with large momentum of k , \mathbf{Q}_d or both, as shown in Fig. 3(g)-(i) respectively. The experimental results do not exhibit any discernible superstructural signals.

Even so, our investigation uncovers intriguing signals. Unraveling the origin of these signals holds promise in gaining insights into the underlying mechanism governing CuBr_2 . To explore the complex characteristics of these scattering signals, we conduct calculations of the X-ray scattering intensity including TDS. Fig. 3(j)-(l) presents the calculated scattering intensity corresponding to the regions depicted in Fig. 3(g)-(i). Importantly, these calculations are performed on a lattice without tetramerized deformation. Notably, the calculated results faithfully replicate all signals observed in the experimental data, with the exception of minor noise. This comparative analysis between the experiment and calculations indicate the absence of lattice deformations.

For additional details, we scan along the diagonal of Fig. 3(i), as shown in Fig. 4. This examination

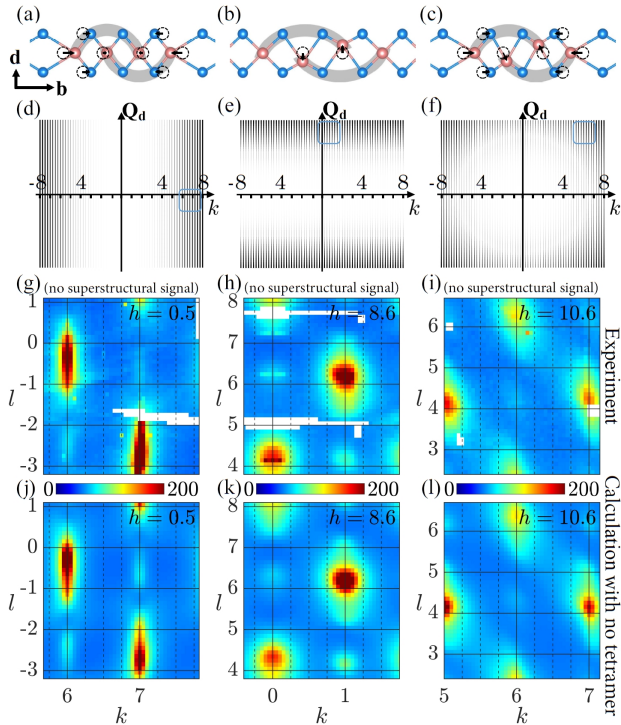


FIG. 3. Analysis of the hard X-ray scattering data. (a)-(c) depict three possible type of atomic displacements of tetramers - (a) along \mathbf{b} , (b) along \mathbf{d} , and (c) in $\mathbf{b}-\mathbf{d}$ plane. The dashed circles indicate original atomic positions. (d)-(f) present the estimated distributions of superstructural signals corresponding to (a)-(c). h , k , l are defined in $\mathbf{Q} = h\mathbf{a}^* + k\mathbf{b}^* + l\mathbf{c}^*$. Q_d represents the momentum projection along \mathbf{d} , approximately parallel to $(\mathbf{a}^* + \mathbf{c}^*)$. The blue rectangles represent the areas of (g)-(i), which respectively depict the experimental intensity at 75 K for large k , large Q_d , and both. (j)-(l) present the calculations corresponding to (g)-(i) with no deformations. The intensity unit is sr^{-1} . No superstructural signal at $k = N/4$ is detected anywhere in the experiment.

reveals four distinctive peaks near $K = 5.5, 6, 6.5, 7$, each displaying distinct temperature-dependent variations. Upon validation, it becomes evident that the peaks near $K = 6, 7$ primarily consist of low-order TDS, while those at $K = 5.5, 6.5$ are dominated by high-order TDS. Hence, relying solely on first-order TDS calculations proves insufficient for accurately reproducing the peaks around $K = 5.5, 6.5$. Consequently, the calculation of high-order TDS is essential in this study.

Through the calculations present in this study, we faithfully replicate all the peaks within this dataset, marking a substantial advancement in TDS calculation methodologies. Utilizing the peaks near $K = 5.5, 6.5$ as guideposts to map the distribution of high-order TDS signals within the reciprocal space, we trace their origin to the constancy of the nearest Cu-Br distance, confirming the presence of a Cu-Br co-

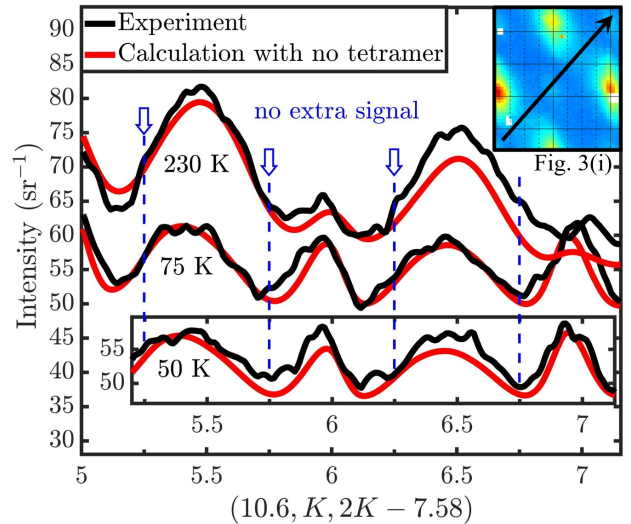


FIG. 4. Comparison between experimental and calculated data at various temperatures. The scanning route is the diagonal from the bottom-left to the upper-right of Fig. 3(i) as shown in the upper-right inset. The experiment agree well with the calculation. No extra signal was detected at $k = N/4$ in the experimental data.

valent bond in CuBr_2 .

It is worth emphasizing that the calculated data match the experimental data across different temperatures, faithfully reproducing the four peaks and their temperature-dependent behavior observed in the experiment, providing strong evidence of their trivial nature. Importantly, no extra signal is detected at $k = N/4$.

We perform a hard X-ray scattering experiment on CuBr_2 , aligning with TDS calculations excluding tetramers. Results show no evidence of tetramers or spin singlets.

B. Neutron total scattering

To detect and analyze the potential tetramerized deformations, we conduct neutron total scattering experiments on CuBr_2 and examine the $g(r)$ data presented in Fig. 5. The data reveals multiple distinct peaks, each corresponding to one or several kinds of atomic distance.

Starting at approximately 2.41 \AA , the first peak signifies the nearest Cu-Br bonds. The second peak at around 3.08 \AA represents the interchain Cu-Br distance. The integral area of each peak reveals the coordination number. Notably, the second peak varies at higher temperatures due to the weakness of the interchain Cu-Br bond. Weak bonds are unable to endure the thermal vibrations of atoms, resulting in broader peaks at higher temperatures.

Our focus is on the third peak, which is located at approximately 3.44 \AA . This particular peak consists

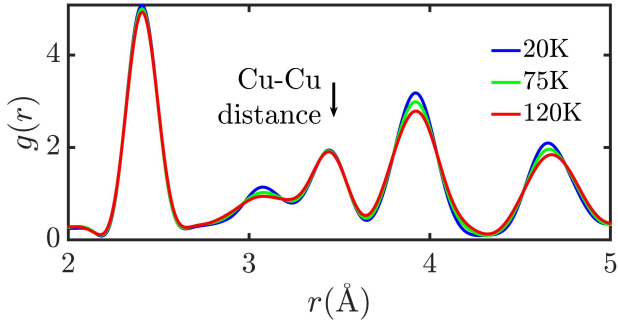


FIG. 5. The pair distribution function of CuBr_2 from the neutron total scattering. No splitting of the Cu-Cu distance is observed.

of three different types of atom pairs: the Br-Br pair along \mathbf{d} , the nearest Br-Br pair along \mathbf{b} , and the nearest Cu-Cu pairs along \mathbf{b} . If tetramerized deformation occurs, at least one of the three components in the third peak would split.

However, upon analyzing Fig. 5, there are no significant temperature-dependent changes observed in the height or width of the third peak. This observation implies the absence of splitting within any of the three components, thereby indicating the lack of significant deformations.

Our analysis of the neutron total scattering data yields insights, but the characteristics of PDFs do not present any evidence supporting the existence of tetramers or spin singlets within our detection sensitivity.

IV. DISCUSSION AND CONCLUSION

The scattering experiments have yielded negative results. Despite the absence of superstructural signals in hard X-ray scattering, it is important to explore the potential presence of singlets distributed in a highly random manner. While such a distribution may not give rise to superstructural signals, it could lead to a shorter correlation length and broader Bragg peaks with Lorentzian shapes. It is essential to determine whether the Bragg peaks will indeed exhibit Lorentzian shapes and reach their maximum width in the proximity of T_N .

We conduct a scan of the (1,7,1) Bragg peak in the hard X-ray data, as depicted in Fig. 6. We discover that the peaks could be well-described by Gaussian functions, without any convolution of Lorentzian functions. This finding suggests that the widths of the peaks are primarily influenced by the measurement conditions rather than the changes of correlation length. Thus, any possible lattice disorder, if exists, is below our detection limit.

The investigation of CuBr_2 yielded no evidence of non-magnetic tetramerized order. The underly-

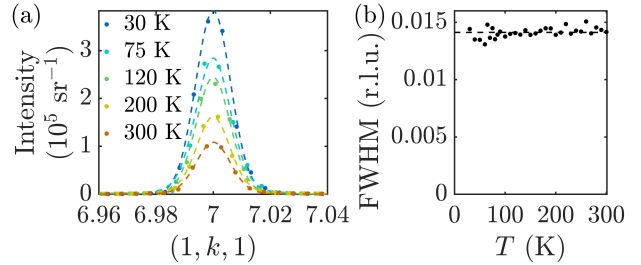


FIG. 6. (a) k -scan of the Bragg peak (1,7,1) at various temperatures. The dashed lines represent Gaussian fits. (b) The corresponding full widths at half maximum (FWHM) extracted from the Gaussian fits. The FWHMs remain consistent at various temperatures, with the mean value indicated by the dashed line. These results suggest that any lattice disorder, if present, is minor.

ing mechanism behind the unusual Raman modes in CuBr_2 remains to be understood.

It is supported by multiple studies that magnetoelastic coupling may arise from the hybridization between magnons and phonons [35, 36], which is the other explanation for the unusual Raman modes in CuBr_2 [22]. The presence of magnon-phonon hybridization may lead to the appearance of Raman peaks in the spectrum, corresponding to the energies of the exciting magnons [22]. The temperature dependence of the magnetic order and the thermal excitation of phonons are opposite, which allow the magnon-phonon hybridization exhibits a non-monotonic relationship with temperature. This scenario provides a plausible explanation for the non-monotonic signals in the Raman data of CuBr_2 .

In recent years, there has been a growing body of evidence indicating the occurrence of magnon-phonon hybridization in a wide range of low-dimensional materials. Noteworthy instances include FePS_3 [37, 38], FePSe_3 [39], and MnPSe_3 [40]. These materials have exhibited distinct Raman peaks below their respective T_N , akin to the partial Raman broad peaks observed in CuBr_2 (*e.g.*, the broad peak near 30 meV). CuBr_2 , being a quasi-one-dimensional antiferromagnet with an effective dimension lower than that of two-dimensional materials. It is reasonable to believe that magnon-phonon hybridization is likely to occur in CuBr_2 .

In order to assess the validity of the magnon-phonon hybridization scenario, we carried out experiments encompassing both time-of-flight neutron scatterings and polarized neutron scatterings. The results do not contradict the concept of magnon-phonon hybridization.

In conclusion, our experimental findings do not substantiate the hypothesis positing the existence of spin singlets in CuBr_2 , as there is a consistent absence of magnetoelastic deformation across multiple conducted experiments. Instead, our findings suggest that the magnetoelastic coupling in the chain com-

pound CuBr_2 is more plausibly ascribed to magnon-phonon hybridization. This conclusion suggests new research paths in phononics and low-dimensional quantum magnetism.

ACKNOWLEDGMENTS

We would like to express our sincere appreciation for the valuable discussions with Hanteng Wang, Hongru Ma, Yiran Liu and Xiquan Zheng. Additionally, we extend our gratitude to the generous support from Junliang Sun's group for providing access to the freeze dryer equipment. The hard X-ray scattering research used resources of the Advanced Photon Source, a U.S. Department of Energy Office of Science User Facility operated for the DOE Office of Science by Argonne National Laboratory under Contract No. DE-AC02-06CH11357. The neutron experiments at the Materials and Life Science Experimental Facility of the J-PARC are performed under a user program (Proposal No. 2019B0377). We acknowledge financial support by the National Natural Science Foundation of China (Grant No. 11874069). These funding sources have played an essential role in advancing our research efforts.

APPENDIX

Appendix A: Calculation of hard X-ray scattering

The relationship between the measured hard X-ray scattering intensity and the cross section can be expressed as

$$\frac{IL^2}{I_0 \cos^3 2\theta} = \frac{d\sigma}{d\Omega} = Nr_e^2 (\sin^2 \phi + \cos^2 \phi \cos^2 2\theta) S, \quad (\text{A1})$$

where I is the photon-number illuminance on the detector, I_0 is the photon-number flux of the incident X-ray, L is the distance from the sample to the detector plane, 2θ is the scattering angle, $\frac{d\sigma}{d\Omega}$ is the differential scattering cross section, N is the number of the atoms participating in the scattering, r_e is the classical electron radius ($r_e \approx 2.82$ fm), and ϕ is the azimuth angle between the polarization plane of the incident beam and the scattering plane. The data collected directly in the experiment is the photon-number illuminance I . Using Eq. A1, I can be transformed into S , whose unit is sr^{-1} . The constants of L , I_0 , r_e , etc. are inessential. By comparing the experimental S in an arbitrary unit with the calculated S in sr^{-1} , the normalization coefficient can be obtained.

Theoretically, S contains both the coherent scattering S_{coh} and the incoherent scattering (*i.e.*, Compton

modified scattering [28]) S_{inc} that [29]

$$S = S_{\text{coh}} + S_{\text{inc}}. \quad (\text{A2})$$

If all electrons are assumed to be the same, then [29]

$$S_{\text{inc}} = \frac{1}{\nu} \sum_{d=1}^{\nu} \left(Z_d - \frac{f_d^2}{Z_d} \right), \quad (\text{A3})$$

where Z_d is the total number of electrons around an atom (or ion) and $Z_d = f_d(Q=0)$, that $Z_{\text{Cu}^{2+}} = 27$ and $Z_{\text{Br}^-} = 36$. S_{coh} can be expanded as [31]

$$S_{\text{coh}} = \sum_{p=0}^{\infty} S_p. \quad (\text{A4})$$

From Eq. 1, A2, A4, it can be derived that

$$S = S_0 + S_{\text{TDS}} + S_{\text{inc}}. \quad (\text{A5})$$

S_0 is Bragg scattering and only appears at Γ points. Following the reference [31], S_0 can be derived as

$$S_0 = \frac{1}{\nu} \left| \sum_{d=1}^{\nu} f_d e^{i\mathbf{Q} \cdot \mathbf{r}_d} e^{-W_d} \right|^2 \frac{(2\pi)^3}{V} \delta(\mathbf{Q} - \mathbf{G}), \quad (\text{A6})$$

where \mathbf{G} is the momentum of the closest Γ point to \mathbf{Q} , V is the volume of a primitive cell, and δ is a 3-dimensional delta function satisfies $\iiint \delta(\mathbf{q}) dq_x dq_y dq_z = 1$. The shape and width of the δ function depend on the sample and the instrument.

Since S_0 only appear at Γ points, the total diffuse scattering intensity is

$$S_{\text{dif}} = S - S_0 = S_{\text{TDS}} + S_{\text{inc}}, \quad (\text{A7})$$

where S_{TDS} is an infinite series as Eq. 1. With the help of the reference [31], we derive S_p as

$$S_p = \frac{1}{\nu} \frac{1}{p!} \left\langle \sum_{j_1=1}^{3\nu} \cdots \sum_{j_p=1}^{3\nu} \left| \sum_{d=1}^{\nu} f_d e^{i\mathbf{Q} \cdot \mathbf{r}_d} e^{-W_d} \prod_{m=1}^p F_{\mathbf{q}_m j_m d} \right|^2 \right\rangle, \quad (\text{A8})$$

where m is the serial number of the phonon, $\langle \cdots \rangle$ here means the average for all the situations that satisfy $\sum_{m=1}^p \mathbf{q}_m = \mathbf{Q}$, and

$$F_{\mathbf{q}j d} = (\mathbf{Q} \cdot \mathbf{e}_{\mathbf{q}j d}) \sqrt{\frac{\hbar \coth \frac{\hbar \omega_{\mathbf{q}j}}{2k_B T}}{2M_d \omega_{\mathbf{q}j}}}, \quad (\text{A9})$$

where $\omega_{\mathbf{q}j}$ is the vibrating frequency, and $\mathbf{e}_{\mathbf{q}j d}$ is a 3×1 complex vector that denotes the direction and relative phase of the j -th vibration mode for the d -th atom within the primitive cell. The displacement from the equilibrium position for the d -th atom within the l -th primitive cell, \mathbf{u}_{ld} , can be expressed with $\mathbf{e}_{\mathbf{q}j d}$ as

$$\mathbf{u}_{ld} = \sum_{\mathbf{q}, j} \mathbf{a}_{\mathbf{q}j d} e^{i\mathbf{q} \cdot \mathbf{R}_l - i\omega_{\mathbf{q}j} t} \quad (\text{A10})$$

$$= \frac{1}{\sqrt{M_d}} \sum_{\mathbf{q}, j} c_{\mathbf{q}j} \mathbf{e}_{\mathbf{q}j d} e^{i\mathbf{q} \cdot \mathbf{R}_l - i\omega_{\mathbf{q}j} t}, \quad (\text{A11})$$

where \mathbf{R}_l denotes the position of the l -th primitive cell, $\mathbf{a}_{\mathbf{q}jd}$ is the amplitude vector and $c_{\mathbf{q}j} = \sqrt{\sum_d M_d |\mathbf{a}_{\mathbf{q}jd}|^2}$.

$\mathbf{e}_{\mathbf{q}jd}$ could be derived from force constant matrices. For the harmonic approximation, the corresponding equation of the ld -th atom is [31]

$$M_d \ddot{\mathbf{u}}_{ld} = \sum_{l'=1}^{[N/\nu]} \sum_{d'=1}^{\nu} \mathbb{K}_{ll'dd'} \mathbf{u}_{ld}, \quad (\text{A12})$$

where $\mathbb{K}_{ll'dd'}$ is the 3×3 real-valued inter-atomic force constant matrices, describing the stiffness between the ld -th and the $l'd'$ -th atom. $[N/\nu]$ denotes the total number of primitive cells. The force constant matrices can be transformed to the dynamical matrices $\mathbb{D}_{\mathbf{q}}$ as

$$\mathbb{D}_{\mathbf{q}dd'} = \sum_{l'=1}^{[N/\nu]} \frac{\mathbb{K}_{ll'dd'}}{\sqrt{M_d M_{d'}}} e^{i\mathbf{q}(\mathbf{R}_{l'} - \mathbf{R}_l)}, \quad (\text{A13})$$

where the 3×3 matrix $\mathbb{D}_{\mathbf{q}dd'}$ is a component of the $3\nu \times 3\nu$ matrix $\mathbb{D}_{\mathbf{q}}$. Our calculation only considers values of l' up to 39, encompassing the nearest 38 primitive cells ($l' = 2 \sim 39$) of the central primitive cell ($l = 1$). For $l' > 39$, we assume $\mathbb{K}_{ll'dd'}$ to be $\mathbf{0}$. For $l' \leq 39$, $\mathbb{K}_{ll'dd'}$ is calculated through VASP and Phonopy. For a vibrating mode, the frequency $\omega_{\mathbf{q}j}$ and the vibrating directions can be obtained from the eigenvalue and the eigenvector of $\mathbb{D}_{\mathbf{q}}$ that [31]

$$\omega_{\mathbf{q}j}^2 \mathbf{e}_{\mathbf{q}j} = \mathbb{D}_{\mathbf{q}} \mathbf{e}_{\mathbf{q}j}, \quad (\text{A14})$$

where the $3\nu \times 1$ complex-valued vector $\mathbf{e}_{\mathbf{q}j}$ is made up of $\mathbf{e}_{\mathbf{q}jd}$ and $|\mathbf{e}_{\mathbf{q}j}|^2 = \sum_d |\mathbf{e}_{\mathbf{q}jd}|^2 = 1$.

With $F_{\mathbf{q}jd}$, W_d can be expressed as

$$W_d = \frac{1}{2} \left\langle \sum_{j=1}^{3\nu} |F_{\mathbf{q}jd}|^2 \right\rangle_{\mathbf{q}}, \quad (\text{A15})$$

where $\langle \dots \rangle_{\mathbf{q}}$ means the average for all the \mathbf{q} in the first Brillouin zone. As shown in Eq. 1, there are infinite terms of S_p for S_{TDS} , so the remainder term R_n is needed. From Eq. A8, A15, the approximate value of S_p can be derived as

$$S_p \approx \frac{1}{\nu} \sum_{d=1}^{\nu} f_d^2 e^{-2W_d} \frac{(2W_d)^p}{p!}. \quad (\text{A16})$$

The approximate remainder term can be derived as

$$R_n = \sum_{p=n+1}^{\infty} S_p \approx \frac{1}{\nu} \sum_{d=1}^{\nu} f_d^2 e^{-2W_d} \sum_{p=n+1}^{\infty} \frac{(2W_d)^p}{p!}, \quad (\text{A17})$$

which can be derived to Eq. 2. By applying Eq. 1 utilizing the expression for R_n as given in Eq. 2, the value of S_{TDS} can be readily obtained.

Subsequently, the diffuse scattering S_{dif} can be derived from Eq. A7, Eq. 1, Eq. 2, and Eq. A3. Notably, when $n = 0$, S_{dif} can be calculated as

$$S_{\text{dif}}^{(n=0)} = \frac{1}{\nu} \sum_{d=1}^{\nu} \left[f_d^2 (1 - e^{-2W_d}) + Z_d - \frac{f_d^2}{Z_d} \right], \quad (\text{A18})$$

which is the reported approximate formula for diffuse scattering at high temperatures [41]. The result is more accurate with larger n . In this research, we successfully calculate with $n = 5$.

* hubiaoyan@quantumsc.cn

- [1] C. Hees, Heat conduction in low-dimensional quantum magnets, *The European Physical Journal Special Topics* **151**, 73 (2007).
- [2] P. Lemmens, G. Güntherodt, and C. Gros, Magnetic light scattering in low-dimensional quantum spin systems, *Physics Reports* **375**, 1 (2003).
- [3] D. D. Sheka, V. P. Kravchuk, and Y. Gaididei, Curvature effects in statics and dynamics of low dimensional magnets, *Journal of Physics A: Mathematical and Theoretical* **48**, 125202 (2015).
- [4] A. Vasiliev, O. Volkova, E. Zvereva, and M. Markina, Milestones of low-D quantum magnetism, *npj Quantum Materials* **3**, 18 (2018).
- [5] H. Bethe, *Zur theorie der metalle*, *Zeitschrift für Physik* **71**, 205 (1931).
- [6] S. Aplesein, Static and dynamic magnetic properties

- of coupled spin-1/2 antiferromagnetic chains, *Journal of Physics: Condensed Matter* **12**, 8191 (2000).
- [7] J. Kokalj, J. Herbrych, A. Zheludev, and P. Prelovšek, Antiferromagnetic order in weakly coupled random spin chains, *Physical Review B* **91**, 155147 (2015).
- [8] Y.-R. Shu, M. Dupont, D.-X. Yao, S. Capponi, and A. W. Sandvik, Dynamical properties of the $S = \frac{1}{2}$ random Heisenberg chain, *Physical Review B* **97**, 104424 (2018).
- [9] S. Sahling, G. Remenyi, C. Paulsen, P. Monceau, V. Saligramam, C. Marin, A. Revcolevschi, L. Regnault, S. Raymond, and J. Lorenzo, Experimental realization of long-distance entanglement between spins in antiferromagnetic quantum spin chains, *Nature Physics* **11**, 255 (2015).
- [10] F. Haldane, Spontaneous dimerization in the $S = \frac{1}{2}$

- heisenberg antiferromagnetic chain with competing interactions, *Physical Review B* **25**, 4925 (1982).
- [11] G. Wellein, H. Fehske, and A. P. Kampf, Peierls dimerization with nonadiabatic spin-phonon coupling, *Physical Review Letters* **81**, 3956 (1998).
- [12] F. Becca, F. Mila, and D. Poilblanc, Tetramerization of a frustrated spin-1/2 chain, *Physical Review Letters* **91**, 067202 (2003).
- [13] H. Nishimori, K. Okamoto, and M. Yokozawa, Competition between the Néel and the effective singlet states in spin-1/2 alternating Heisenberg-Ising antiferromagnet in one dimension, *Journal of the Physical Society of Japan* **56**, 4126 (1987).
- [14] H. Yamase and H. Kohno, Competition and coexistence between Néel order and d-wave singlet RVB, *Physica C: Superconductivity* **408-410**, 273 (2004).
- [15] P. W. Anderson, The resonating valence bond state in La_2CuO_4 and superconductivity, *Science* **235**, 1196 (1987).
- [16] P. W. Anderson, G. Baskaran, Z. Zou, and T. Hsu, Resonating-valence-bond theory of phase transitions and superconductivity in La_2CuO_4 -based compounds, *Physical Review Letters* **58**, 2790 (1987).
- [17] P. W. Anderson, P. Lee, M. Randeria, T. Rice, N. Trivedi, and F. Zhang, The physics behind high-temperature superconducting cuprates: the ‘plain vanilla’ version of RVB, *Journal of Physics: Condensed Matter* **16**, R755 (2004).
- [18] E. Ninomiya, M. Isobe, Y. Ueda, M. Nishi, K. Ohoyama, H. Sawa, and T. Ohama, Observation of lattice dimerization in spin-singlet low temperature phase of $\text{NaTiSi}_2\text{O}_6$, *Physica B: Condensed Matter* **329**, 884 (2003).
- [19] G. Deng, M. Kenzelmann, S. Danilkin, A. J. Studer, V. Pomjakushin, P. Imperia, E. Pomjakushina, and K. Conder, Coexistence of long-range magnetic ordering and singlet ground state in the spin-ladder superconductor $\text{SrCa}_{13}\text{Cu}_{24}\text{O}_{41}$, *Physical Review B* **88**, 174424 (2013).
- [20] C. M. Pasco, I. El Baggari, E. Bianco, L. F. Kourkoutis, and T. M. McQueen, Tunable magnetic transition to a singlet ground state in a 2D van der Waals layered trimerized kagomé magnet, *ACS nano* **13**, 9457 (2019).
- [21] I. L. Danilovich, E. V. Karpova, I. V. Morozov, A. V. Ushakov, S. V. Streltsov, A. A. Shakin, O. S. Volkova, E. A. Zvereva, and A. N. Vasiliev, Spin-singlet quantum ground state in zigzag spin ladder $\text{Cu}(\text{CF}_3\text{COO})_2$, *ChemPhysChem* **18**, 2482 (2017).
- [22] C. Wang, D. Yu, X. Liu, R. Chen, X. Du, B. Hu, L. Wang, K. Iida, K. Kamazawa, S. Wakimoto, *et al.*, Observation of magnetoelastic effects in a quasi-one-dimensional spiral magnet, *Physical Review B* **96**, 085111 (2017).
- [23] L. Zhao, T.-L. Hung, C.-C. Li, Y.-Y. Chen, M.-K. Wu, R. K. Kremer, M. G. Banks, A. Simon, M.-H. Whangbo, C. Lee, *et al.*, CuBr_2 – a new multiferroic material with high critical temperature, *Advanced Materials* **24**, 2469 (2012).
- [24] R.-Q. Wang, J.-C. Zheng, T. Chen, P.-S. Wang, J.-S. Zhang, Y. Cui, C. Wang, Y. Li, S. Xu, F. Yuan, *et al.*, NMR evidence of charge fluctuations in multiferroic CuBr_2 , *Chinese Physics B* **27**, 037502 (2018).
- [25] A. Apostolov, I. Apostolova, and J. Wesselinowa, CuBr_2 , *Journal of Magnetism and Magnetic Materials* **560**, 169633 (2022).
- [26] C. Lee, J. Liu, M.-H. Whangbo, H.-J. Koo, R. Kremer, and A. Simon, Investigation of the spin exchange interactions and the magnetic structure of the high-temperature multiferroic CuBr_2 , *Physical Review B* **86**, 060407 (2012).
- [27] S. Lebernegg, M. Schmitt, A. A. Tsirlin, O. Janson, and H. Rosner, Magnetism of CuX_2 frustrated chains ($X = \text{F}, \text{Cl}, \text{Br}$): the role of covalency, *Phys. Rev. B* **87**, 155111 (2013).
- [28] B. E. Warren, *X-ray diffraction* (Addison-Wesley Publishing Company, 1969).
- [29] R. W. James, *The optical principles of the diffraction of X-rays* (George Bell & Sons, 1962).
- [30] J. Als-Nielsen and D. McMorrow, *Elements of modern X-ray physics* (John Wiley & Sons, 2011).
- [31] A. Q. Baron, Introduction to high-resolution inelastic X-ray scattering, arXiv:1504.01098 (2015).
- [32] P. Brown, A. Fox, E. Maslen, M. O’Keefe, and B. Willis, Intensity of diffracted intensities, *International Tables for Crystallography C*, 554 (2006).
- [33] D. A. Keen, A comparison of various commonly used correlation functions for describing total scattering, *Journal of Applied Crystallography* **34**, 172 (2001).
- [34] S. J. Billinge and C. L. Farrow, Towards a robust ad hoc data correction approach that yields reliable atomic pair distribution functions from powder diffraction data, *Journal of Physics: Condensed Matter* **25**, 454202 (2013).
- [35] B. Liu, H. Xiao, G. Siemann, J. Weber, B. Andres, W. Bronsch, P. M. Oppeneer, and M. Weinelt, Signature of magnon polarons in electron relaxation on terbium revealed by comparison with gadolinium, *Physical Review B* **104**, 024434 (2021).
- [36] S. Zhang, G. Go, K.-J. Lee, and S. K. Kim, $\text{SU}(3)$ topology of magnon-phonon hybridization in 2D antiferromagnets, *Physical Review Letters* **124**, 147204 (2020).
- [37] S. Liu, A. G. Del Águila, D. Bhowmick, C. K. Gan, T. T. H. Do, M. Prosnikov, D. Sedmidubský, Z. Sofer, P. C. Christianen, P. Sengupta, and Q. Xiong, Direct observation of magnon-phonon strong coupling in two-dimensional antiferromagnet at high magnetic fields, *Physical Review Letters* **127**, 097401 (2021).
- [38] D. Vaclavkova, M. Palit, J. Wyzula, S. Ghosh, A. Delhomme, S. Maity, P. Kapuscinski, A. Ghosh, M. Veis, M. Grzeszczyk, *et al.*, Magnon polarons in the van der Waals antiferromagnet FePS_3 , *Physical Review B* **104**, 134437 (2021).
- [39] J. Luo, S. Li, Z. Ye, R. Xu, H. Yan, J. Zhang, G. Ye, L. Chen, D. Hu, X. Teng, *et al.*, Evidence for topological magnon-phonon hybridization in a 2D antiferromagnet down to the monolayer limit, *Nano Letters* **23**, 2023 (2023).
- [40] T. T. Mai, K. F. Garrity, A. McCreary, J. Argo, J. R. Simpson, V. Doan-Nguyen, R. V. Aguilar, and A. R. H. Walker, Magnon-phonon hybridization in 2D antiferromagnet MnPS_3 , *Science Advances* **7**, eabj3106 (2021).
- [41] G. Harvey, Diffuse scattering of X-rays from Sylvine. IV. Scattering at high temperatures, *Physical Review* **44**, 133 (1933).